Variations in Bounding and Scanning Relative Permeability Curves With Different Carbonate Rock Types

M.R. Dernaika, SPE, Ingrain Incorporated–Abu Dhabi; **M.A. Basioni, A. Dawoud,** and **M.Z. Kalam,**
Abu Dhabi Company for Onshore Oil Operations (ADCO); and **S.M. Skjæveland,** SPE, University of Stavanger

Summary

Relative permeability curves generally exhibit hysteresis between different saturation cycles. This hysteresis is mainly caused by wettability changes and fluid trapping. Different rock types may experience different hysteresis trends because of variations in pore geometry. Relative permeability curves may also be a function of the saturation height in the reservoir.

A detailed laboratory study was performed to investigate relative permeability behavior for a major carbonate hydrocarbon reservoir in the Middle East. Representative core samples covering five reservoir rock types (RRTs) were identified on the basis of whole core and plug X-ray computed tomography (CT), nuclear magnetic resonance (NMR) T2, mercury injection capillary pressure (MICP), porosity, permeability, and thin-section analyses. Primary-drainage (PD) and imbibition water/oil relative permeability (bounding) curves were measured on all the five rock types by the steady-state (SS) technique by use of live fluids at full reservoir conditions with in-situ saturation monitoring (ISSM). Imbibition relative permeability experiments were also conducted on the main RRT samples to assess the relative permeability (scanning) curves in the transition zone (TZ) by varying connate-water saturations.

Hysteresis effects were observed between PD and imbibition cycles, and appeared to be influenced by the sample rock type involved (i.e., wettability and pore geometry). Variations in relative permeability within similar and different rock types were described and understood from local heterogeneities present in each individual sample. This was possible from dual-energy (DE) CT scanning and high-resolution imaging. Different imbibition trends from both oil and water phases were detected from the scanning curves that were explained by different pore-level fluid-flow scenarios. Relative permeability scanning curves to both oil and water phases increased with higher connate-water saturation. Relative permeability to oil was explained on the basis of the occupancy of the oil phase at varying connate-water saturations. The change in the water relative permeability trend was addressed on the basis of the connectivity of water at the varying connate-water saturations. These results and interpretations introduced an improved understanding of the hysteresis phenomena and fluid-flow behavior in the TZ of a Cretaceous carbonate reservoir that can assist in the overall reservoir modeling and well planning.

Introduction

Relative permeability (K_r) can be used for estimating productivity, injectivity, hydrocarbons in place, breakthrough time, and ultimate recovery (Honarpour et al. 1986, 1995; Heaviside 1991). Relative permeability curves depend on the direction of saturation changes as well as on the maximal and minimal achieved saturations (Jerauld and Salter 1990; Masalmeh 2001). Hysteresis in relative permeability curves can exist between different saturation cycles. Most experimental studies in literature have found that hysteresis is large for the nonwetting phase and either small or

nonexistent for the wetting phase. Much of the hysteresis data in the literature has been obtained with bounding curves; saturations starting at endpoint values (i.e., irreducible water and residual oil saturations for water/oil systems). Hysteresis is also studied with scanning curves in which the direction of saturation change is reversed at a number of intermediate saturations. Data such as these are applicable for modeling reservoir processes in which the water saturation increases or decreases to an intermediate value, then changes in the opposite direction. Hysteresis is mainly caused by contact-angle hysteresis, fluid trapping, and wettability changes. Contact-angle hysteresis is usually attributed to nonequilibrium effects, contamination, or heterogeneity of the surface because of either roughness or composition. Fluid trapping is a result of pore-space geometry and is caused by instabilities in the fluid/fluid interface configurations. Wettability is the overall tendency of a reservoir rock to prefer one fluid over another, and depends on rock pore-size distribution and rock/fluid interactions.

Relative permeability is also a function of pore geometry (Fatt 1966; Morgan and Gordon 1969). There are certain rock properties that affect pore geometry and can have a great influence on reservoir properties such as porosity, permeability, capillary pressure, relative permeability, and resistivity. **Table 1** lists some of the main rock properties that are considered important in carbonate reservoirs. These rock properties are interrelated and thus may exert different effects in different rock types. Therefore, it is not sufficient to characterize a reservoir rock by a single datum such as porosity or permeability. Proper rock characterization will be necessary to understand variations in rock types that, in turn, help relate variations in macroscopic measurements (e.g., relative permeability curves) to rock properties and pore geometry.

In this paper, we present experimental hysteresis in relative permeability (bounding) curves between primary drainage and imbibition on five different carbonate rock types. Imbibition relative permeability experiments were also conducted on the main RRT samples to assess the relative permeability (scanning) curves in the TZ by varying connate-water saturations. The rock types were initially characterized by static rock typing that is based on petrophysical data and geological description. The relative-permeability measurements were performed by the SS technique at full reservoir conditions by use of live fluids with ISSM. These experiments were used to study the effect of different carbonate rock types on relative permeability and hysteresis trends. Such data are rather scarce in the literature because most of the available data are either measured on water-wet rocks or on limited rock types. The hysteresis data provided in this work are needed to enrich the available hysteresis models that may lack a complete and consistent description of the hysteresis phenomena in porous media.

Throughout this paper, drainage is used to describe oil displacing water. Imbibition describes water displacing oil regardless of wettability condition. PD is used to represent oil displacing water from 100% water saturation. Spontaneous imbibition refers to water displacing oil in water-wet pores, and forced imbibition is used to refer to imbibition in mixed-wet pores.

Rock Characterization

The rock (micro) properties that control pore geometry determine many macroscopic properties of the porous medium. Establishing

TABLE 1—MAIN ROCK PROPERTIES THAT AFFECT PORE GEOMETRY IN CARBONATES

Pore System (intergranular, intercrystalline, vuggy, fractured)
Pore (Throat) Size (relative presence and distribution)
Aspect Ratio (Pore body to pore throat)
Pore Configuration (surface area, tortuosity)
Particulate System (sorting, shape, packing)

the relation between the microproperties and macroscopic physical properties of a rock sample is an essential requirement in the understanding of fluid-flow behavior and saturation distribution in porous media and in the production of oil and gas from petroleum-bearing reservoirs. If variations in rock types are ignored, laboratory measurements for predicting fluid flow may be misleading (Morgan and Gordon 1969).

In this study, RRTs were initially established on the basis of combined petrophysical properties and geological description. The petrophysical properties included measurements from porosity, permeability, NMR T2 distributions, and mercury-derived drainage capillary pressure (P_c) and pore-throat-size distribution (PSD). Geological descriptions were obtained from thin-section photomicrographs analysis that aims at defining pore systems, facies, and depositional environment. Mercury injection and thin-section preparation were performed on corresponding trims from the plug samples. To enhance our rock-characterization scheme, high-definition X-ray DE CT scanning was acquired on the plugs not only to investigate the internal structure of the rocks through CT images but also to quantify mineralogy and porosity along sample lengths through X-ray CT-derived effective atomic number (Z_{eff}) and bulk density (BD) (Wellington and Vinegar 1987). Such knowledge of rock fabric and mineralogical distribution is an essential input for reservoir modeling and well planning (Pranter et al. 2005).

The used core plugs in this study were 1.5 in. in diameter and approximately 3 in. in length. All samples were CT scanned at two energy levels with calibration material. The images were acquired in helical high-resolution scanning mode and have an in-plane (X–Y) pixel resolution of 0.468 mm and a slice thickness (Z) of 0.500 mm. This DE imaging provides two distinct 3D images of the plugs. The high-energy images are more sensitive to BD, and the low-energy images are more sensitive to mineralogy. The method summarized by Wellington and Vinegar (1987) was used to compute independently the BD and the Z_{eff} for each CT slice position for every plug. The Z_{eff} parameter is related to the photoelectric effect (PEF) commonly used in wellbore logging. Thus, profiles of BD/Z_{eff} as well as plug averages are generated and used for quality assurance, rock typing, and heterogeneity assessment.

Figs. 1 and 2 provide a rock-characterization scheme from five different RRTs found in the reservoir. **Fig. 3** gives the porosity/permeability variation for all the samples, and **Fig. 4** shows the crossplot of Z_{eff} vs. BD and grain density. Both Z_{eff} and BD were derived from the DE CT scanning, whereas the grain-density values were measured in a conventional laboratory in combination with helium porosity. Fig. 3 shows an interesting behavior of the best rock type (RRT1) samples. Those samples have the highest permeability values and yet are at the lower end of the porosity range within all the rock types. This is a heterogeneity feature in carbonates and, in this case, it is attributed to dolomitization that caused the recrystallization of the limestone mineral, resulting in larger pores and pore throats, better connectivity, and increased pore heterogeneity. The lower porosity from RRT1 samples must be because of the bigger grain size for dolomite.

Fig. 4 (to the left) plots the average Z_{eff}/BD values from all plugs. All samples lie on the calcite line except RRT1 samples that come close to the dolomite Z_{eff} line. The BD data give sample porosity with grain-density information that could be inferred from the Z_{eff} or simply from laboratory measurement. **Table 2** gives BD and Z_{eff} for three major minerals (i.e., calcite, dolomite, and quartz).

The Z_{eff}/grain density (GD) plot in Fig. 4 shows that the calcite samples gave laboratory grain-density values at 2.71 g/cm^3 as compared with the dolomite samples that gave higher grain densities.

In Fig. 1, individual porosity/permeability data are given above each thin-section photomicrograph for direct comparison. The CT images are presented in color scale with reference to the color-scale bar on top of the CT images in Fig. 1b. Normally, X-ray CT images come in shades of gray, which are directly influenced by the Z_{eff} of the material and its density. Dense material such as calcite appears white, and pores appear black. Unresolved pores such as micrite would appear as dark gray. Such gray-scale images may not always show all the detailed internal features; thus, we prefer to present the images in a color-scale format in which dense materials appear red and pores appear black. Any material density varying in between would appear as yellow or green on the basis of the color-scale bar shown in the figure. It is worth noting that the same color scale was applied to all images so that it becomes possible to have a one-to-one comparison between the different rock-type images and between images in the same rock type to evaluate local heterogeneity and to better assess overall quality. This is actually another important feature of the use of color-scale images.

In Fig. 2, two reference lines are shown on the NMR T2 plots to allow direct comparisons with the other rock-type curves. A reference line is also shown on the mercury-derived PSD curves for the same reason. NMR T2 data give information about pore-body-size distribution and can be converted to a length unit by use of the surface-relaxation parameter. On the other hand, mercury-intrusion data do not provide direct information about pore diameters; they rather assign the pore-body volumes to their entry throats. Therefore, mercury data contain valuable information about reservoir rocks and rock types because the resistance offered by the pore structure to fluid flow is controlled by the pore throats.

In Fig. 2, we see a general trend in the entry pressure that is increasing as we move from RRT1 through RRT5. This is normally because of the macro pore sizes decreasing as we move toward the poorer-quality rock types. However, we see that all rock types are showing a similar range of irreducible saturation (at 1,000-psi mercury pressure, equivalent to 75 psi oil/water P_c). This is because all samples do not have many pore-throat radii less than 0.1 μm as can clearly be seen in the Hg-derived PSD curves. Nevertheless, the samples would have differences in the intermediate pore-throat sizes, and this is demonstrated on the P_c curves for each RRT in which the intersections of the curves at a 200-psi pressure have been shaded to see how this shaded area is occurring at lower mercury (corresponding to oil in reservoir-fluid system) saturations as we move toward RRT5. This observation proves that the different RRTs have varying intermediate pore-throat sizes that can yield differences in capillary pressures and phase flow.

The importance of this rock-characterization phase and the way we present the rock types in Figs. 1 and 2 lie on the local variations identified in each sample and how this variation could play a role in producing different macroscopic measurements such as relative permeability functions and hysteresis patterns. A summary of the rock-characterization scheme is presented in **Table 3**.

Rock Type 1. A thin-section description of RRT1 samples reveals the dolomitic nature of those samples. Sample 113 (with a 46-md permeability) is fine-to-medium crystalline dolomite with vugs and intercrystalline meso- to macropores. It has a loosely packed texture, and this explains its higher permeability value than Sample 114 (with 21 md). Sample 114 is a strongly dolomitized packstone with intercrystalline micro- to macropores. Its matrix microporosity has been reduced in places by intensive dolomitization. In both thin-section photomicrographs, the dolomite grains have a gray color, pores are in blue, and (minor) blocky calcite cement can be seen in red. The corresponding CT images in Fig. 1b confirm the heterogeneity seen in the porosity/permeability data and clearly show the large connected pore channels along plug lengths.
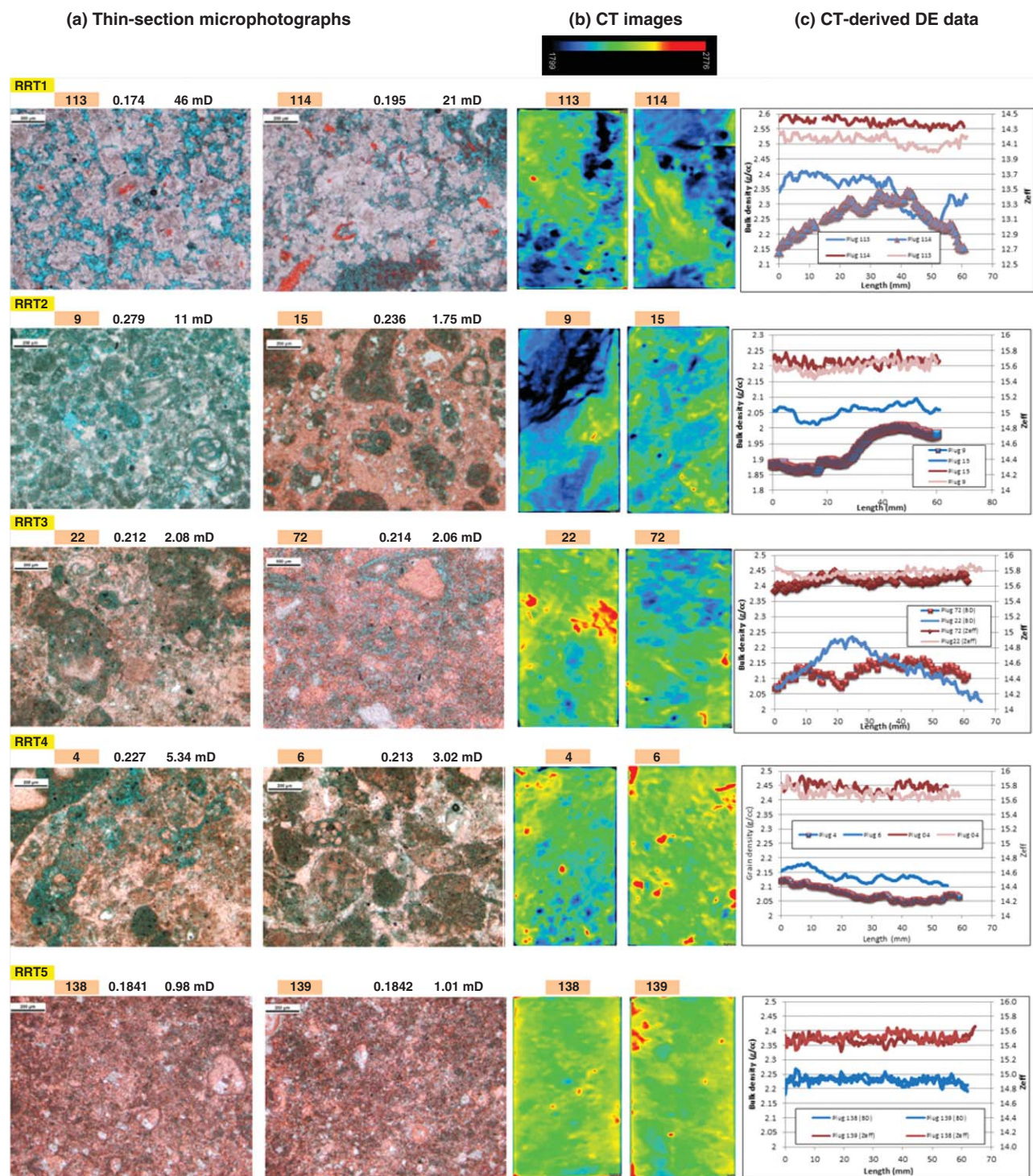
(a) Thin-section microphotographs   **(b) CT images**   **(c) CT-derived DE data**

Fig. 1—(a) Thin-section photomicrographs. (b) Color-scale CT images at 500 μm/pixel (color scale bar in pixels is shown on top of the images). The middle longitudinal CT slice is shown here. (c) X-ray CT-derived DE BD and Z_{eff} data along sample lengths. Two plugs are selected for each rock type. There are five different rock types identified in the reservoir. Sample number and porosity/permeability data are shown above each thin-section photomicrograph. Sample number is also identified above each CT image.

The X-ray CT-derived DE data along sample lengths (i.e., BD and Z_{eff}) are given in Fig. 1c. The Z_{eff} (mineralogy) distributions reveal uniform profiles, whereas BD curves show high pore heterogeneity along sample lengths.

Rock Type 2. In Fig. 1a, the thin-section description of RRT2 samples reveals the calcitic nature of those samples. Sample 9 (with 11-md permeability) is grainstone with intraparticle porosity in the micrite and interparticle intercrystalline porosity. Sample 15 (1.75 md) is a grainstone to rudstone showing shell debris and heterogeneous texture with intraparticle porosity in the micrite.

The corresponding CT images on the whole plugs in Fig. 1b present consistent observations to the thin-sections and show that Sample 9 has large pore channels, as revealed in the large area of low pixels (i.e., blue color) in the relevant image. On the other hand, Sample 15 has a larger proportion of the higher pixels (green/yellow colors) distributed along the sample length that hinders the flow in the large pore channels.

The DE data plot confirms these observations and yields a lower BD (i.e., higher porosity) distribution for Sample 9. Both samples give a uniform Z_{eff} distribution of approximately 15.7, confirming the calcitic nature of those samples. The fracture seen
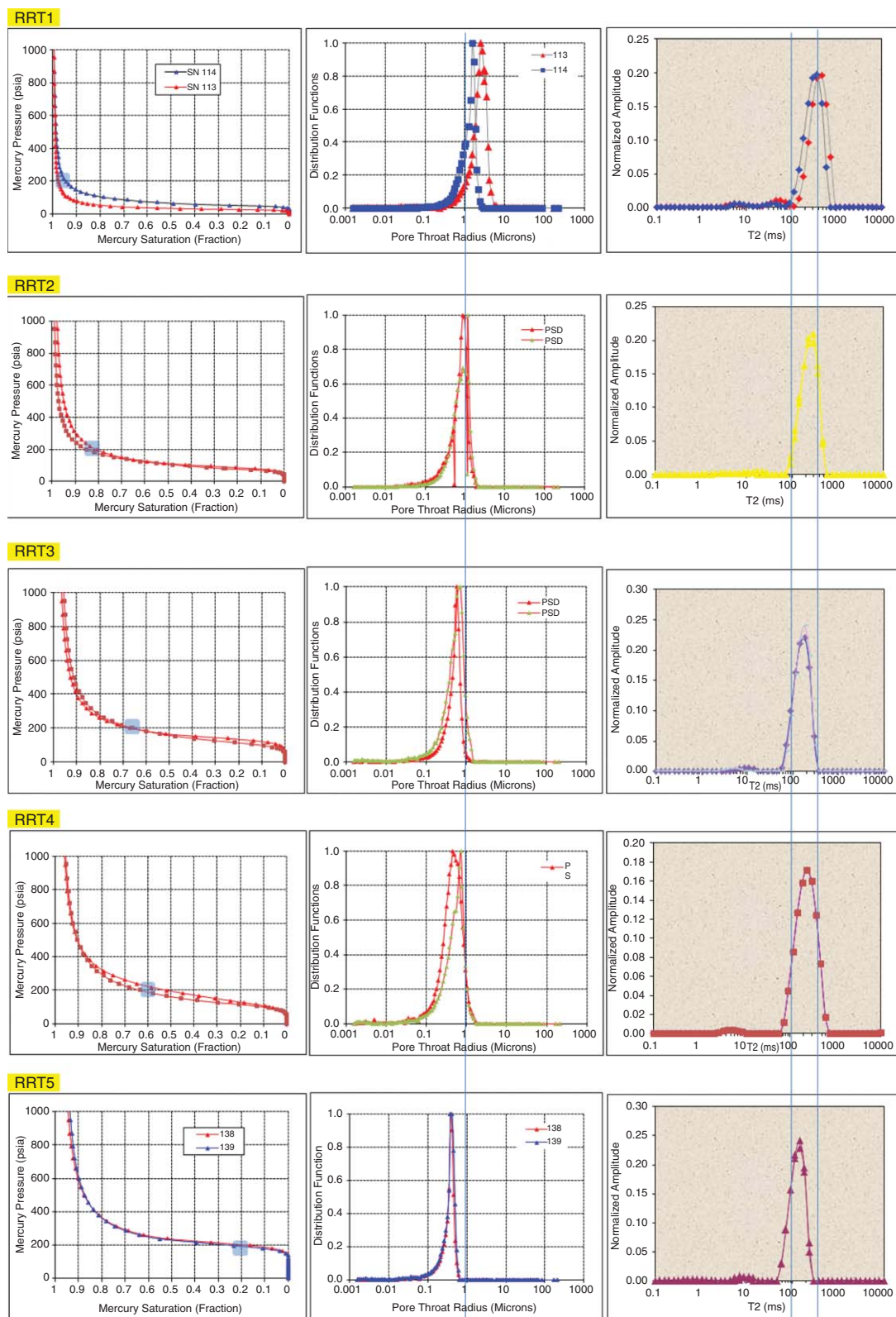
Fig. 2—Two plots to the left, respectively: Mercury-derived drainage capillary pressure (P_c) and PSD. The P_c curves are shown with shaded squares at 200 psi to emphasize the variation of rock properties within the different rock types. The plot to the right: NMR T2 distributions on 100% brine-saturated plugs. Reference lines are added on the distribution plots to follow property changes with rock types. Two plugs are selected for each rock type. There are five different rock types identified in the reservoir.

at the top of the CT image of Sample 9 was induced by the implementation of improper procedures that were performed after the relative permeability experiments were completed. The reason we are showing the image is to confirm that indeed Sample 9 has different pixel distributions at the plug scale and also to confirm it

has a lower BD that could be inferred from the bottom part of the plug that was not damaged in the laboratory. The permeability and porosity variations between these samples in RRT2 and the earlier observations from CT data may suggest that Sample 15 could be classified better as RRT3.
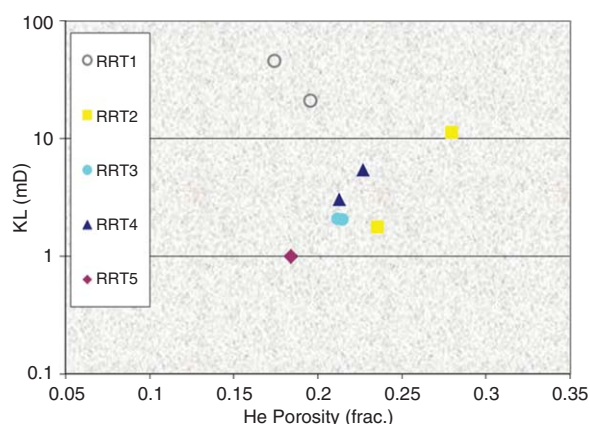
Fig. 3—Permeability vs. porosity for the five different rock types

Rock Types 3 and 4. These two rock types are calcitic and almost similar in nature and distributions, and may actually be classified as one rock type. They are packstone with intraparticle porosity in the micrite. Similar to the previous investigations, we see an interesting consistency between thin-section photomicrographs, CT images, DE data, mercury, and NMR T2 distributions. The main point to emphasize here is the variation in porosity/permeability data that can clearly be linked to the CT color-scale images.

Rock Type 5. The plugs in RRT5 are amazingly similar in every single datum generated or measurement obtained from them. They are calcitic-in-nature, bioturbated packstone with intercrystalline microporosity between microcrystalline calcite cements. Interparticle pore space is reduced by micritic matrix and pore-filling calcite and dolomite cements. They gave the least porosity/permeability data and the most homogeneous BD distributions. One can hardly differentiate between these two samples, and it will certainly be interesting to see how similar the multiphase-flow behavior will be.

Relative Permeability Bounding Curves

Before the start of the relative permeability program, all samples were thoroughly cleaned by flow-through techniques by use of repeated cycles of several hot solvents to render the rocks water-wet (presumed wettability condition before oil entered the reservoir). Each core-plug sample was then saturated with 100% simulated formation water (SFW) that is representative of the reservoir-water composition. PD and imbibition water/oil relative permeability (bounding) curves were measured on all the five rock types by the SS equilibrium fractional flow technique by use of live fluids at full reservoir conditions with gamma ray as ISSM. In each (PD and imbibition) flood, mutually equilibrated SFW and live oil were injected concurrently into the top of every core plug. Injection at fractional flow rate was continued until the pressure and production had stabilized, before altering the fractional flow rate to the next predetermined step. The system again ran until stable pressure and saturation were achieved. The stabilization criteria were no changes in saturation and pressure drop at each step for a few hours. This was repeated for each determined fractional flow rate. **Table 4** gives the water fractions (F_w) used during the PD and imbibition floods. No aging period was designed at the end of each saturation step. The total duration of each flooding cycle took approximately 2 weeks. A high-rate bump flood was performed at the end of each flood. The bump flood is a dramatic increase in the flow rate of the injected phase at the end of the saturation (flooding) cycle to counter capillary end effects. In drainage, the oil-flow rate was increased by 10 times and similarly for the water-flow rate in imbibition. After the oil bump flood at the end of the PD, the core plugs were aged at reservoir conditions for a period of 4 weeks without changing the experimental setup. This testing condition is believed to render the rocks mixed-wet for a representative wettability condition during the following imbibition process. **Table 5** gives flooding rates and capillary numbers for RRT1 and RRT5 samples. The capillary number is given as viscous forces to capillary forces ($N_c = \mu v/\sigma$), where μ stands for viscosity, σ for interfacial tension (IFT), and v for fluid velocity. The same flow rates were used in drainage and imbibition, and the capillary numbers were comparable in both saturation cycles for each RRT. The capillary numbers given in Table 5 are calculated from the imbibition experiments. The flooding rate used for RRT2 through RRT5 samples was 20 cm³/hr. Higher flooding rate (i.e., 30 cm³/hr) was used for the RRT1 samples because of their higher permeability values.

Fig. 5 gives the PD and imbibition relative permeability for all RRT samples. It also gives the hysteresis behavior between the PD and imbibition cycles. Fig. 5a presents the PD relative permeability curves, whereas Fig. 5b presents the imbibition relative permeability curves. Fig. 5c plots the hysteresis curves between primary drainage and imbibition. From each RRT classification, there are two samples. In each plot of Fig. 5a, the two samples from the same RRT are plotted together. Similarly, the imbibition curves from the two samples in each RRT are plotted together in each of the plots in Fig. 5b. On the other hand, Fig. 5c gives each sample data in a different plot for each RRT classification to
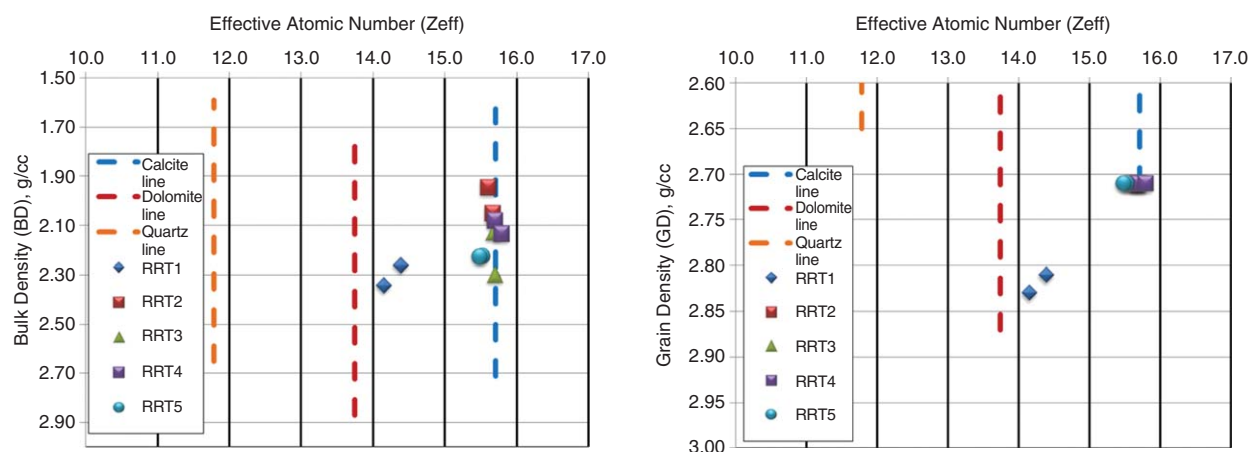

Fig. 4—Plot to the left: Z_{eff} vs. BD for all rock types. Z_{eff} values are indicated for pure calcite, dolomite, and quartz. The CT-derived Z_{eff} values show that RRT1 samples are mostly dolomitic, whereas the other RRT samples are calcitic. Plot to the right: Z_{eff} vs. GD for all rock types. The laboratory-measured GD values for RRT1 samples are in the range of 2.8 to 2.85 g/cm³. This confirms the dolomitic nature of these samples inferred from the X-ray CT-derived Z_{eff} values. Similarly, the other RRT samples give consistent Z_{eff} and GD values, confirming the calcitic nature of the samples.

TABLE 2—BD AND Z_{EFF} FOR CERTAIN PURE MINERALS		
Mineral	BD (g/cm³)	Z_{eff}
Calcite	2.71	15.71
Dolomite	2.85	13.74
Quartz	2.65	11.78

emphasize the hysteresis trend for each plug sample. The saturation cycle (i.e., PD or imbibition) and the sample number and RRT are indicated in the title chart of each plot. This data set aims at comparing the relative permeability behavior between different carbonate rock types found in the reservoir under study. Each row in the figure represents a single rock-type data as classified earlier in Figs. 1 and 2. Actually, Fig. 5 presents the different RRT K_r data in the same fashion as the RRT classification in Figs. 1 and 2 so that direct comparisons can be made between the RRT and the relative permeability behavior.

In the same fashion, **Fig. 6** presents the PD and imbibition in-situ (water) saturation monitoring profiles (ISSM) along sample lengths for all RRT samples. Each saturation profile represents equilibrium water saturation at the end of each fractional flow rate that was used during the SS relative permeability experiment. These ISSM curves are necessary to check the quality of the relative permeability curves. Two main features are normally detected from such curves: heterogeneity and capillary end effect. A bump flood was designed at the end of each saturation cycle to establish more-uniform water saturation (S_w) along sample lengths. The S_w

profiles after the bump floods are monitored through the ISSM curves. The saturation cycle (i.e., PD or imbibition) and sample number and RRT are indicated in the title charts. Before the oil bump flood is made in drainage, the S_{wi} profile may appear non-uniform because of a capillary end effect. This situation may severely affect the subsequent imbibition data. It is seen in Fig. 6 that the bump floods reduced the capillary end effects and made the S_{wi} profiles look less affected. The uniformity of the saturation profiles should always be taken into consideration for reliable relative permeability data. Such data could also be better qualified by use of coreflood numerical simulation, which is discussed in a later section in the paper.

Primary Drainage. In Fig. 5a, we see little differences between the PD relative permeability (K_r) curves between the samples in the same RRT. These differences seem to become smaller as we move toward the poorer-quality RRT samples. The differences are obviously caused by local heterogeneity that is seen more in higher-permeability carbonate samples that are characterized by vugs, moldic porosity, and diversified ranges of micro- to macropores. There is no clear relation between the K_{rw}/K_{ro} intersection (saturation) point and rock type in Fig. 5a. However, all the intersection points for all the rock-type samples seem to be in the range of a 0.55 through 0.65 water saturation.

In Fig. 5a, Sample 113 (in the RRT1 plot) suffered from a large capillary end effect that caused the K_{ro} curve to flatten at a lower water saturation (S_w). This can be seen clearly in the corresponding ISSM curves in Fig. 6. The bump flood at the end of drainage decreased the water saturation further and gave a more

TABLE 3—SUMMARY OF THE ROCK-CHARACTERIZATION SCHEME										
Sample Number	RRT	Thin-Section Description	Mineral	Z_{eff}	GD (g/cm³)	BD Profile	Porosity (fraction)	Permeability (md)	Hg Saturation at 200 psi (fraction)	Micron at the Peak of PSD	T2 at NMR Peak (milliseconds)
113	1	Vugs and inter-crystalline meso to macropores (loosely packed texture)	Dolomite	14.14	2.83	Non-uniform	0.174	46	0.97	2.7	373
114	1	Intercrystalline micro- to macropores	Dolomite	14.39	2.81	Non-uniform	0.195	21	0.95	1.53	295
9	2	Interparticle porosity, intraparticle porosity in micrite (grainstone)	Calcite	15.59	2.70	Non-uniform (from CT image)	0.279	11	0.82	1.15	295
15	2	Intraparticle porosity in micrite (grainstone to rudstone)	Calcite	15.66	2.70	Uniform	0.236	1.75	0.82	0.87	294
22	3	Packstone	Calcite	15.76	2.70	Non-uniform	0.212	2.08	0.65	0.72	184
72	3	Packstone	Calcite	15.67	2.70	Non-uniform	0.214	2.06	0.65	0.60	184
4	4	Packstone	Calcite	15.69	2.70	Non-uniform	0.227	5.34	0.52	0.72	233
6	4	Packstone (pores reduced by cement)	Calcite	15.78	2.71	Non-uniform	0.213	3.02	0.62	0.50	233
138	5	Bioturbated packstone (microporosity between cement)	Calcite	15.51	2.73	Uniform	0.184	0.98	0.23	0.42	145
139	5	Bioturbated packstone (microporosity between cement)	Calcite	15.47	2.73	Uniform	0.184	1.01	0.23	0.42	145

TABLE 4—WATER FRACTIONS (F_w) USED DURING PD AND IMBIBITION FLOODS	
F_w in Primary Drainage	F_w in Imbibition
1.00	0.00
0.98	0.02
0.95	0.05
0.85	0.15
0.50	0.50
0.15	0.85
0.05	0.95
0.01	0.99
0.00	1.00

TABLE 5—FLOODING RATES AND CAPILLARY NUMBERS IN THE K_r EXPERIMENTS		
	RRT1	RRT5
Total flooding rate	30 cm^3/hr	20 cm^3/hr
Capillary number ($N_c = \mu v / \sigma$)	6.8×10^{-8}	4.7×10^{-8}

uniform S_w profile. All samples were subjected to a bump flood to produce more-representative saturations. This was necessary because of the capillary end effect, which is basically the saturation gradient along sample lengths, as can be seen in Fig. 6. The capillary end effect is defined as the accumulation of a preferentially wetting phase (i.e., water in PD) at the outlet when displacing the wetting phase by the nonwetting phase (i.e., oil). This observation confirms that the PD experiment was conducted at a preferentially water-wet condition. This, in turn, suggests that the solvent-cleaning procedures implemented at the restoration stage of the samples were efficient.

Without the bump floods, the water saturations at the end of PD range from 0.2 to 0.3. After the bump floods, those saturations decreased to a range of 0.05 to 0.23. Similarly, the K_{ro} increased after the bump flood from a range of 0.2 to 0.5 to a range of 0.65 to 0.85. These changes (i.e., increase in K_{ro} and decrease in S_w) emphasize the importance of the bump-flood design and demonstrate the impact of the capillary end effect on relative permeability curves. Different samples/rock types may experience different magnitudes of capillary end effects because of variations in rock properties. This is especially true for water-wet states in which the significance of the pore geometry is most apparent (Wardlaw 1980).

Imbibition. In Fig. 5b, the imbibition K_r curves are presented in the same fashion as the PD K_r curves in Fig. 5a. The imbibition K_{rw}/K_{ro} intersection points occur at lower Sw values than the intersection points of drainage. The imbibition K_{rw}/K_{ro} intersection points decreased to a range of 0.45 to 0.6. This might be an indication of wettability change to less water-wet conditions (Honarpour et al. 1986), but conclusions about wettability alterations from K_r curves can be risky especially for intermediate- and/or mixed-wet conditions (Cuiec 1991).

Without bump floods, the water saturations at the end of imbibition range from 0.75 to 0.85. After the bump floods, these saturations increase to a range of 0.80 to 0.95. Similarly, the K_{rw} increased after the bump flood from a range of 0.2 to 0.3 to a range of 0.2 to 0.55. Fig. 6 does not show severe end effects in imbibition except for Sample 9 from RRT2 and Sample 22 from RRT3. This can be seen in the relevant ISSM curves that show lower S_w values toward the outlets of the samples. These effects were minimized by the bump floods, as can also be seen in Fig. 6 in the relevant plots.

The ISSM curves for RRT1 samples in Fig. 6 show fluctuations in both drainage and imbibition as compared with the other rock types. This is not noise in the saturation-profile data; it is caused by the local heterogeneity along the lengths of the samples that become apparent in the presence of vugs.

The imbibition K_r curves in Fig. 5b for each of the two samples in each RRT show similar behavior except for minor variations because of local heterogeneity that is basically related to the specific types and relative percentages of pores present, and their distribution within the rock. The similar imbibition behavior of the different samples in the same RRT confirms that the static

rock-typing scheme established from petrophysical measurements and geological descriptions is valid and yields similar imbibition dynamic data for the samples under study. This is an interesting examination of the effect of static rock characterization on the dynamic data and rather important input information for an ultimate dynamic reservoir modeling (Masalmeh 2000). The only violation to this link between static and dynamic rock typing is RRT2 samples that had already been shown to give variations in the static rock characterization between Samples 9 and 15. Although these two samples were initially selected to be RRT2, the reality is that Sample 15 is better fitted into RRT3, as explained previously. This again confirms the consistency established between static and dynamic rock typing. There may not be a guarantee to establish a good link between the static and dynamic rock types because of local heterogeneity and wettability, but proper static rock typing is certainly the way to reduce the discrepancies that may arise between the two rock-typing schemes.

The preceding observations made between PD and imbibition relative permeability characteristics indicate that there were some changes in the wettability conditions of the samples after aging. It is actually expected to observe mixed-wet behavior in such carbonate samples during the imbibition process. This has been indicated by the low remaining oil saturations obtained at the end of imbibition together with the increase in water saturations (from drainage to imbibition) at the K_{rw}/K_{ro} intersection points. In addition, most of the K_{rw} values attained at the end of imbibition suggest mixed-wet behavior (Honarpour et al. 1986; Masalmeh 2001). Nevertheless, the effect of wettability on the relative permeability endpoints is still subject for discussions, and these indications are only rules of thumb that are questioned by several researchers (e.g., Morrow 1990), especially for mixed-wettability systems.

Fig. 7 presents (in semilog scale) relative permeability curves for different rock-type samples to assess the effect of rock types on the relative permeability behavior in PD and imbibition. Figs. 7a and 7b give the PD K_{rw} curves and the PD K_{ro} curves, respectively, whereas Figs. 7c and 7d give the imbibition K_{rw} curves and the imbibition K_{ro} curves, respectively. **Fig. 8** plots Fig. 7 in linear scale. In PD, the curves did not show major variations between the different RRT samples. At the high-water-saturation end, K_{ro} tends to be larger for large pore-sized samples at the start of oil invasion. At the lower-S_w end (i.e., toward the end of drainage), the curves seem to be influenced by capillary end effects. The imbibition curves in Figs. 8c and 8d for both K_{rw} and K_{ro}, respectively, show large variations between the different rock types. One can also detect larger variations in the imbibition water relative permeability than in the imbibition oil relative-permeability curves. This result highlights the fundamental differences between drainage and imbibition fluid-flow mechanisms at the pore level. It also indicates the potential differences in the flow pattern between oil and water.

In Fig. 8c, the larger-pore-sized samples (i.e., RRT1 and RRT2) show higher K_{rw} than the smaller-pore-sized samples (i.e., RRT4 and RRT5) at a given water saturation. In this perspective, RRT1 and RRT2 samples show more oil-wet characteristics than the poorer-quality RRT4 and RRT5 samples. This is also supported by the imbibition K_{ro} trends in Fig. 8d for RRT1 and RRT2 samples, which tend to show a more rapid reduction upon water invasion into the large oil-wet pores. Opposite to the K_{rw} behavior, the large-pore-sized samples (i.e., RRT1 and RRT2) give lower K_{ro} values at a given S_w. All those samples were
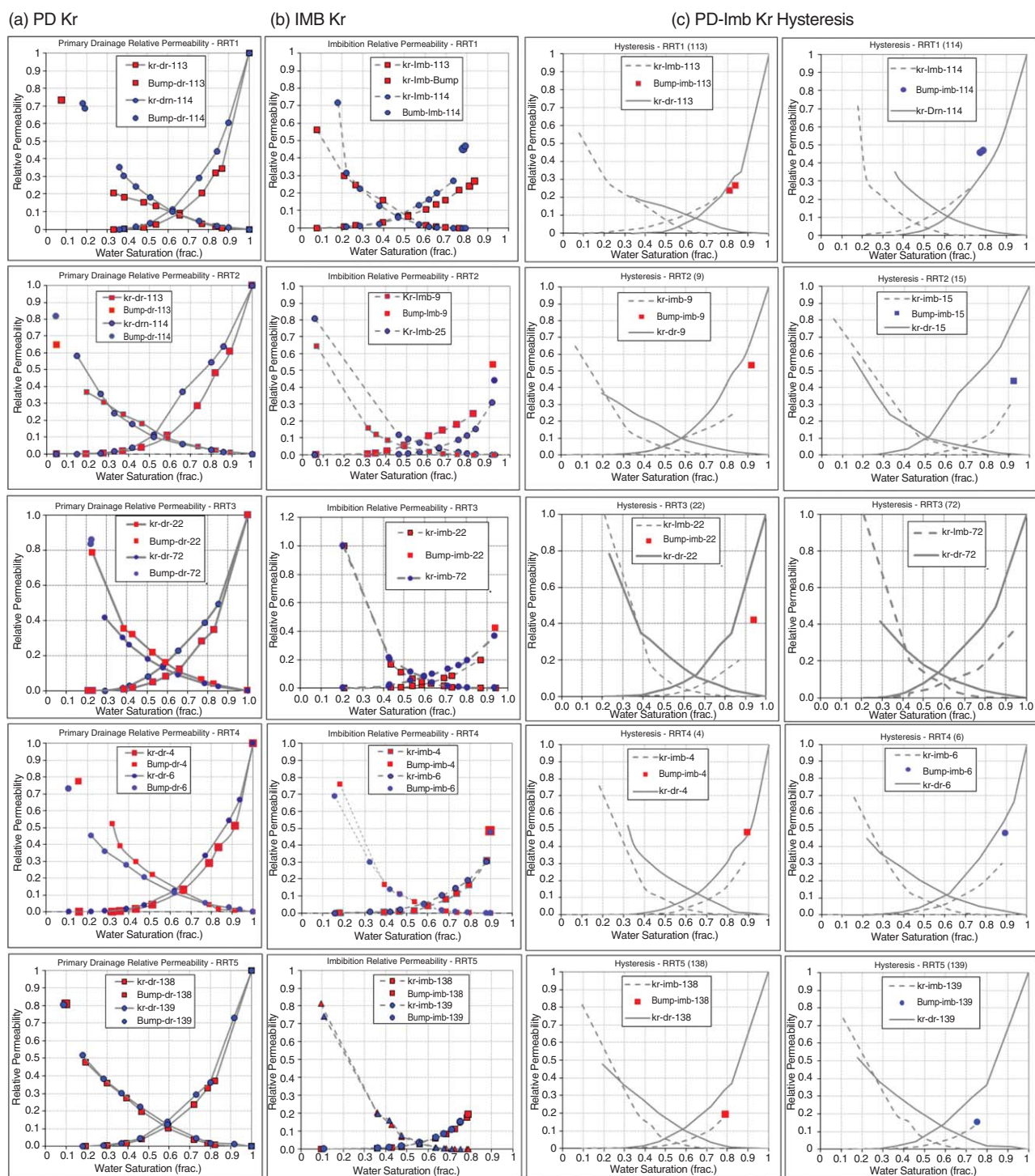
Fig. 5—(a) Primary-drainage K_r curves for all RRTs. (b) Imbibition K_r curves for all RRTs. (c) Hysteresis in the K_r curves between PD and imbibition for all the RRTs. Every plot row presents one rock type, and the RRT number is indicated in the chart title. RRT1 curves gave a different hysteresis trend from the other RRTs.

exposed to the same fluids at the same conditions, and there is no clear reasoning behind possible variations in the wettability conditions between the samples under study. The main differences between those samples are the rock geometrical properties (see Table 1) that tend to give rise to different fluid mechanisms in imbibition more than in PD. This should be the result of a more complex fluid-flow regime in imbibition, as will be explained in the following.

Hysteresis. Fig. 5c shows the hysteresis behavior between PD and imbibition. Each plot presents the K_r curves from one rock

sample to compare between the different saturation cycles. RRT1 samples gave a different hysteresis pattern to all other rock types. In RRT1, the imbibition K_{ro} is lower than the PD K_{ro} curve at the same water saturation, and the imbibition K_{rw} is higher than the PD K_{rw} curve at the same water saturation. For all the other rock types (i.e., RRT2 through RRT5 samples), the imbibition K_{ro} curve is lower than the PD K_{ro} curve (this is a similar behavior to RRT1), but this time the imbibition K_{rw} curve is lower than the PD K_{rw} curve at the same water saturation. Existing hysteresis models (Jerauld and Salter 1990; Masalmeh 2001) would classify RRT1 samples as mixed-wet to oil-wet and the other RRT samples as water-wet. In principle, for the water-wet case, both
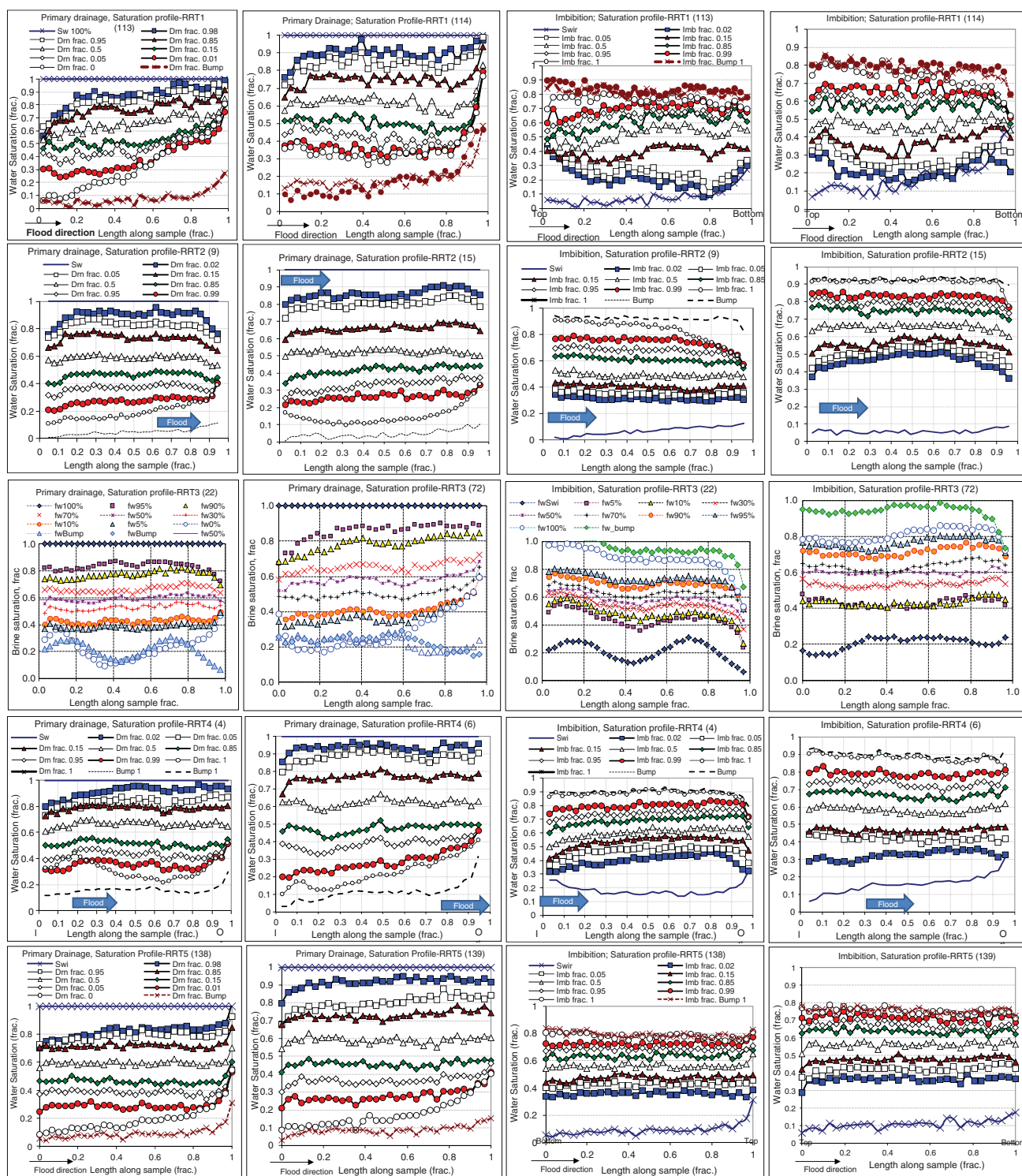
Fig. 6—Primary drainage and imbibition in-situ (water) saturation profiles (ISSM) along sample lengths for all RRT samples. Saturation cycle (i.e., primary drainage or imbibition) and sample number and RRT are indicated in title charts. These ISSM curves are necessary to check the quality of the relative permeability curves reported earlier. Two main features are normally detected from such curves: heterogeneity and capillary end effect.

imbibition relative permeability to oil (K_{ro}) and to water (K_{rw}) are shifted to lower water saturations because of oil trapping that, in turn, causes lower mobile oil saturation. This causes the imbibition K_{ro} to be lower than the PD K_{ro} curve, and will cause the imbibition K_{rw} to be higher than the PD K_{rw}. However, oil trapping may hinder water flow and thus may lead to lower imbibition K_{rw} than the PD K_{rw}. Thus, there will be two opposing effects on the imbibition K_{rw}, which in many cases can cause no major hysteresis in the K_{rw} curve between PD and imbibition in water-wet

systems (Masalmeh 2001). For the mixed-wet case, imbibition will start displacing big oil-wet pores and small water-wet pores. Water will occupy more big pores during imbibition than during PD, and this may lead to a higher imbibition K_{rw} than PD K_{rw} curve. Imbibition K_{ro} will be lower than the PD K_{ro} because there will be fewer large pores occupied with oil. This is a brief explanation of the PD and imbibition hysteresis model on the basis of different wettability scenarios. This explanation seems to be generally consistent with previously published hysteresis trends.
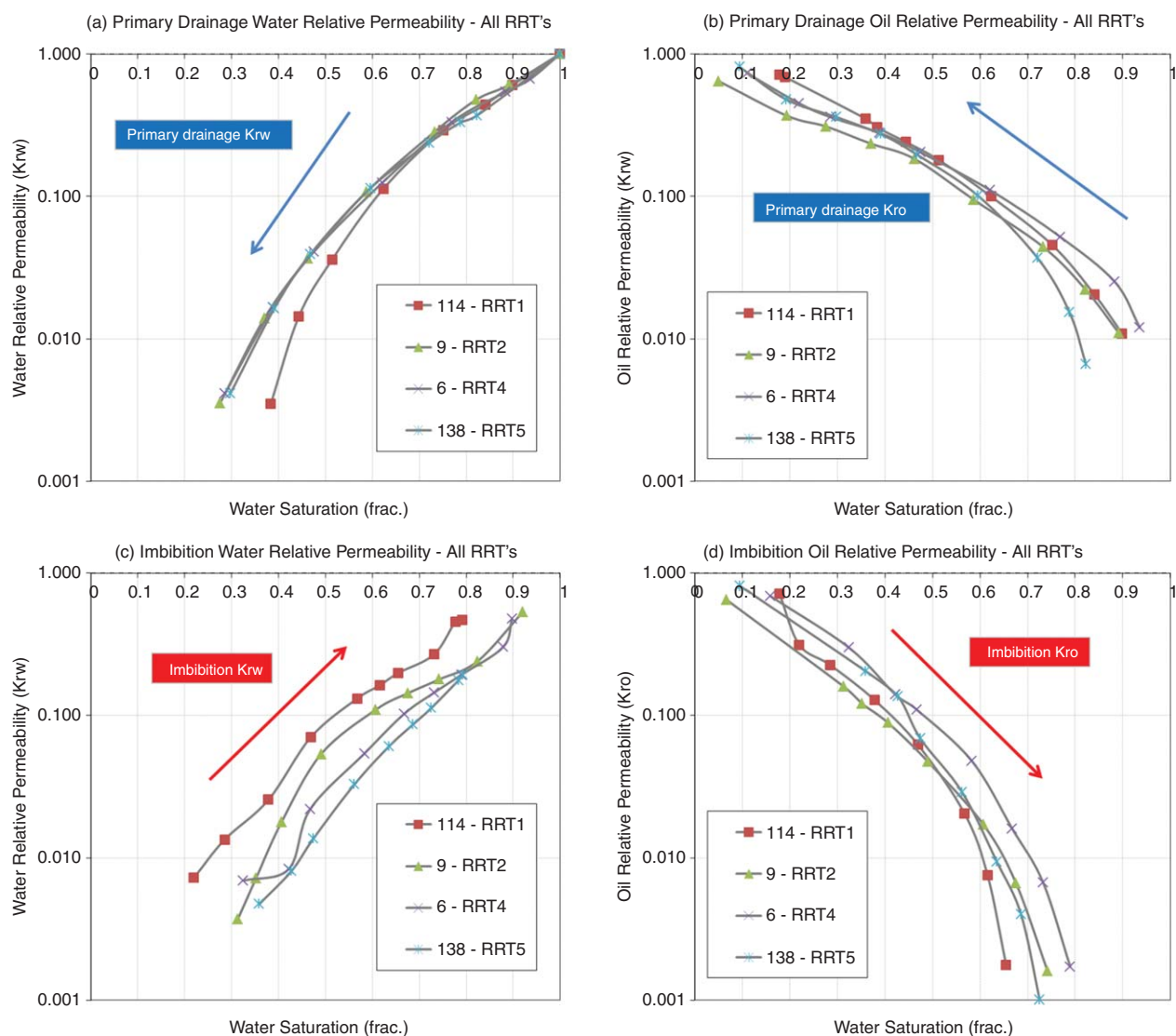
Fig. 7—Relative-permeability curves (semilog plot) for different rock types to assess the effect of rock types on K_r behavior in primary drainage and imbibition. (a) Primary-drainage K_{rw} curves. (b) Primary-drainage K_{ro} curves. (c) Imbibition K_{rw} curves. (d) Imbibition K_{ro} curves. Fig. 8 presents Fig. 7 in linear scale.

However, this model—as with many other introduced models for fluid flow in porous media—needs to be used carefully when judging wettability states out of relative permeability macromeasurements. The reason for this is the lack of a sufficient number of relative permeability experiments performed at full reservoir conditions with live fluids on many different rock types to support this model.

Previous capillary pressure curves measured on similar rock types at reservoir conditions did not show any spontaneous imbibition and indeed showed mixed-wet characteristics from forced imbibition data (Dernaika et al. 2012). Therefore, the different relative permeability hysteresis trends reported in this work must be related to differences in pore geometry between the different rock-type samples in addition to the wettability considerations. There must be combined effects from both pore geometry and wettability that may result in such variations in hysteresis trends.

The Effect of Pore Geometry on Imbibition *Kr* and Hysteresis

The dolomite rock type (i.e., RRT1) has a loosely packed texture with large, open pore-throat sizes, whereas the calcite rock types in this study are mainly cemented with reduced pore-throat sizes. Such a difference in the pore system may yield differences in the

ratio of pore body to pore-throat size, which is commonly referred to as the "aspect ratio." One would normally expect the more loosely packed rock type with large pores and pore throats to have a lower aspect ratio than the calcitic well-cemented samples with small pores. The aspect ratio could also be inferred from the peak values of the T2 curve and the mercury PSD. This can be easily calculated from the given values in Table 3. For RRT1 samples (i.e., 113 and 114), the T2 by PSD peak ratios are 373/2.7(138) and 295/1.53(193), respectively. Sample 9 from RRT2 and Sample 138 from RRT5 would give T2 by PSD peak ratios as 257 and 345, respectively. This clearly shows that the aspect ratio would increase as we move from RRT1 through RRT5. This is not a calculation of the aspect ratio, but it can certainly help understand the change of the aspect ratio with the rock type. The T2 value was used to infer pore-body size. The aspect ratio is one of the most important rock properties of porous media that can influence imbibition behavior: The larger the aspect ratio is, the more fluid trapping occurs that could yield higher degrees of hysteresis (Jerauld and Salter 1990; Morrow et al. 2008). On the basis of this analysis, the RRT2 through RRT5 samples with a higher aspect ratio may have experienced more oil trapping in imbibition.

In addition to the aspect ratio, the accessibility of individual pores contributes to the flow behavior and to the magnitude of permeability. Fluids do not seem to invade individual pores as set
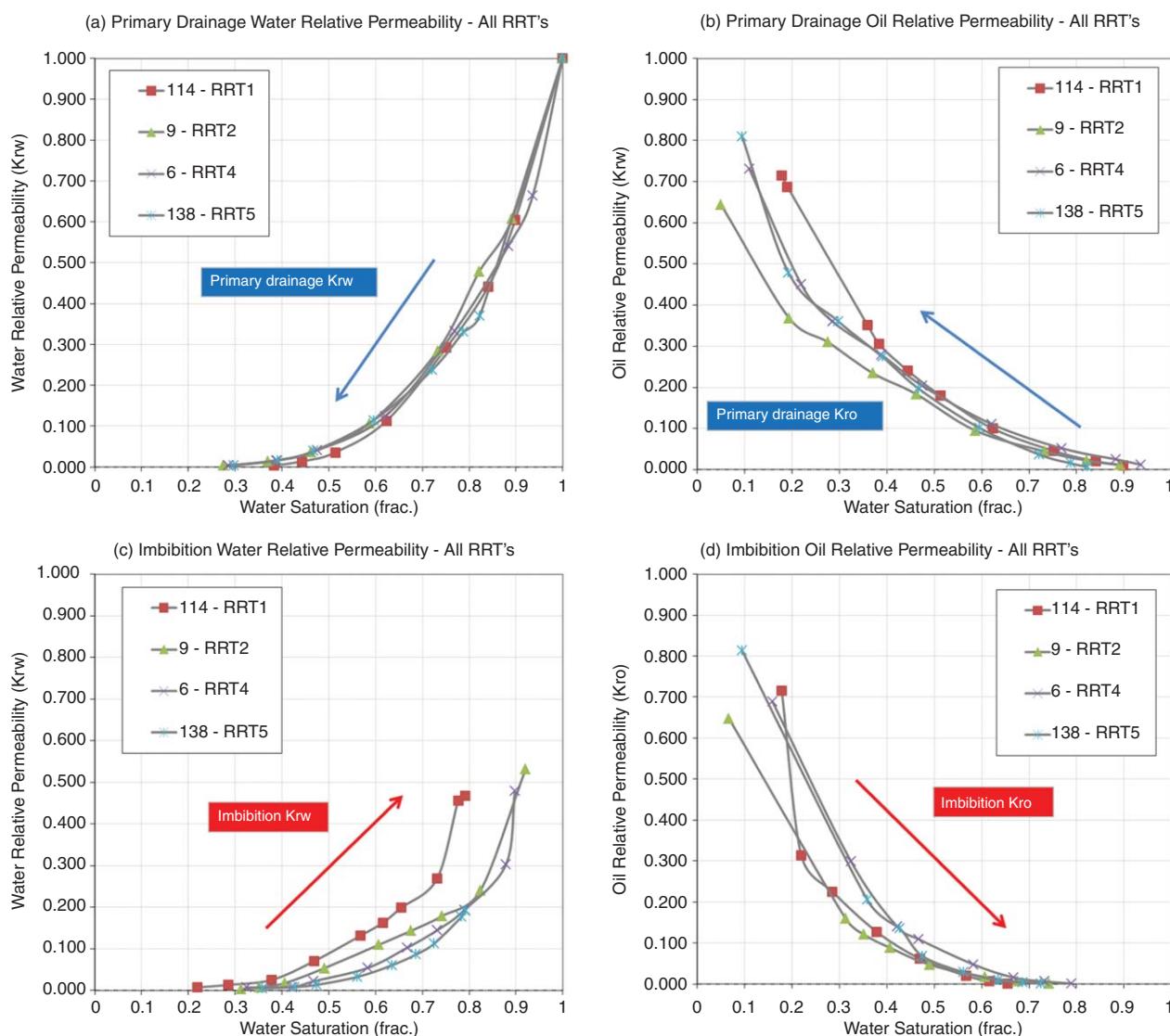
Fig. 8—Relative-permeability curves (linear scale of Fig. 7) for different rock types to assess the effect of rock types on K_r behavior in primary drainage and imbibition. (a) Primary-drainage K_{rw} curves. (b) Primary-drainage K_{ro} curves. (c) Imbibition K_{rw} curves. (d) Imbibition K_{ro} curves.

by the entry pressures of the corresponding pore throats. Invasion often occurs in large clusters (Yuan 1991), and therefore the size of the pore throats and the number of pore throats emanating from a pore body (often called coordination number) largely affect the accessible interconnections in the pore system. Smaller-pore-sized systems may reduce the accessibility of individual pores and thus may yield higher invasion pressures that may result in smaller magnitudes of permeability. In imbibition, lower accessibility of individual pores may promote the trapping of oil clusters that eventually may hinder water flow. This could be another reason for the lower K_{rw} in imbibition with poorer-quality RRT samples and the resultant hysteresis trend.

Moreover, the pore corners and crevices in which water is still present remain water-wet. The area of the water-wet surface would be comparable to all pores invaded by the oil (Helland and Skjæveland 2005). This would mean that the established water-wet surface area is expected to be almost the same for all invaded pores between RRT1 and RRT2 through RRT5 samples. Thus, the smaller pores in the calcite rocks would have a larger fraction of water-wet surface, and should therefore exhibit a more water-wet behavior than the larger pores in RRT1 during imbibition.

It is actually obvious from Fig. 5 that RRT5 samples with the smallest pore and pore-throat sizes have shown the most water-wet imbibition K_r behavior on the basis of existing hysteresis

models (**Figs. 7 and 8).** This does not necessarily mean that this RRT5 is water-wet. It shows water-wet behavior because of the combined effects of wettability and pore geometry. To emphasize this argument, similar RRT samples have been measured in porous plate at reservoir conditions and did not show any positive capillary pressure imbibition. Similar RRT samples were also tested in wettability-index experiments, and they gave large negative values that ranged from −0.55 to −0.66, indicating mixed-wet states.

Previous researchers had commented on the risk of evaluating the wettability of a reservoir solely from relative permeability curves because of the heterogeneous nature of wettability and the uncertain degree of wettability alterations (Torsaeter 1988; Cuiec 1991). This analysis of pore geometry and wettability behavior has been useful in explaining the variations seen in the hysteresis patterns among the various rock types involved. This same analysis helps explain the variations of the imbibition K_{ro} and K_{rw} curves in Figs. 7 and 8.

Relative Permeability Scanning Curves

At the top of the TZ, big pores and small pores are invaded with oil, whereas at the bottom of the TZ, only the big pores may be invaded with oil; the smaller pores there would stay filled with
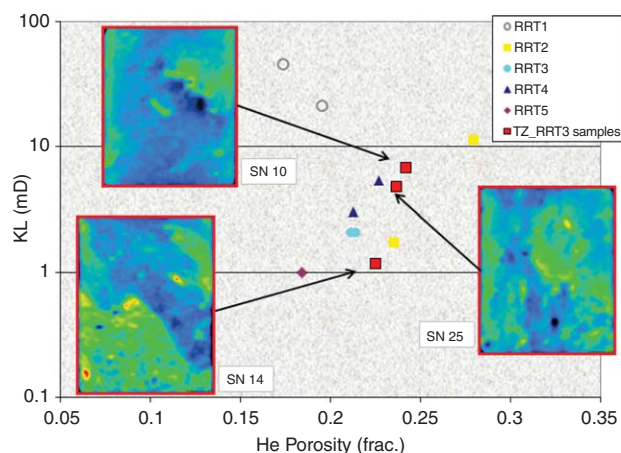
Fig. 9—Permeability vs. porosity for the five different rock types in the K_r bounding-curve program including three TZ samples in the K_r scanning-curve program with their corresponding CT images and SNs. The CT images are a good representation of the porosity/permeability variations seen in the TZ samples.

Fig. 10—Oil relative permeability imbibition scanning curves for the TZ samples from RRT 3. Additional imbibition K_{ro} curve from RRT3 (i.e., SN 22) bounding curve is plotted to compare with a wider range of S_{oi} values. Each imbibition curve starts from different initial oil saturation (S_{oi}) to investigate fluid-flow behavior in the reservoir TZ.

water and would remain water-wet. This would yield variations in the wettability state (along the length of the TZ), which are governed by the increase in water saturation with depth. One would expect more oil-wet rocks at the top of the TZ (i.e., low S_{wi} as compared with the base of the zone in which the rocks should be more water-wet. Such variations in saturations and wettability can have a large impact on the production characteristics along the depth of the TZ (e.g., Masalmeh 2000).

Three plug samples (10, 5, and 14) from the main RRT 3 were selected to undergo fractional flow SS relative permeability experiments to investigate the imbibition K_r behavior in the TZ of the reservoir under study. The experiments were performed at representative conditions to simulate reservoir behavior. Each sample starting with 100% S_w was prepared to different target initial oil saturation (S_{oi}) by a PD SS K_r experiment with a total flow rate of 20 cm³/hr. Depending on the target S_{oi} among the three samples, different water fractional flow rates (F_w) were used. Plug 10 reached a target initial oil saturation of 0.32 by use of 0.95 F_w; Plug 25 reached a target S_{oi} of 0.52 by use of 0.30 F_w; and Plug 14 reached a target S_{oi} of 0.68 by use of 0.05 F_w. When the target S_{oi} value was reached, the PD was stopped, and the samples were aged at the established saturations in crude oil at reservoir temperature for 4 weeks before the imbibition process was started. The
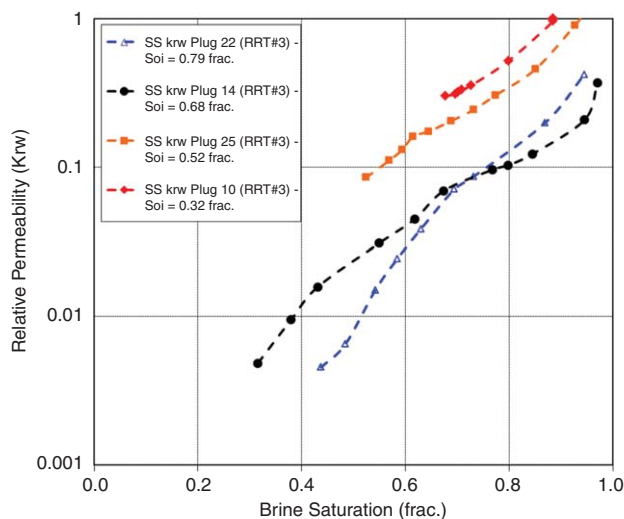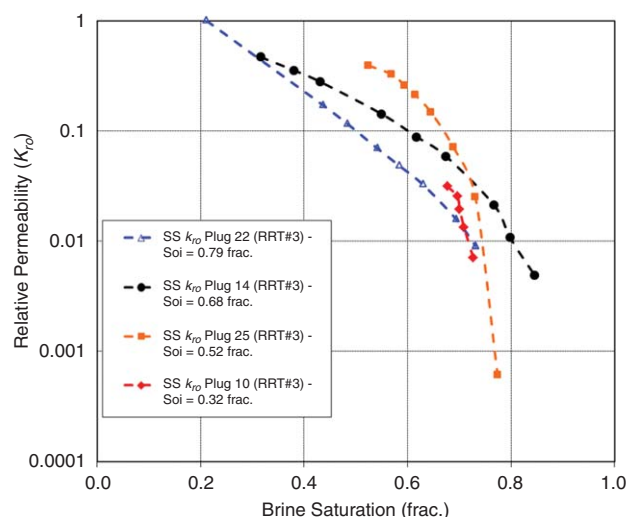
total flow rate of 20 cm³/hr was also used in imbibition. The water fractional flow rate for each sample was different and started from the F_w at which the drainage cycle was stopped. The imbibition scanning relative permeability experiment followed the same procedure as the bounding K_r experiments described previously. Approximately eight fractional flow rates were used with increasing water fractions up to 1 F_w. The phase-flow rate and measured SS differential pressure were used to calculate the individual effective phase permeability, which, in turn, was used to calculate relative permeability with the absolute permeability value as the reference permeability.

Fig. 9 shows the porosity/permeability data for the three TZ samples together with the porosity/permeability data from the K_r bounding-curve program. The figure also presents the corresponding CT images and sample numbers (SNs) from the TZ rock samples. The CT images confirm the porosity/permeability variations seen in the TZ samples. In Fig. 10, Plug 10 started with the lowest initial oil saturation (S_{oi}) of 0.32, followed by Plug 25 ($S_{oi} = 0.52$), and finally Sample 14 ($S_{oi} = 0.68$). The bounding imbibition fractional flow K_{ro} curve (Plug 22) is also shown in the figure for reference and to investigate the imbibition K_{ro} scanning-curve behavior in a wider saturation range. It would certainly be more representative to carry out the scanning-curve experiments (at varying S_{oi}) on one plug, but this would lead to extensive time delays in the project timing.

The tests appear to show trends of increasing K_{ro} with decreasing initial oil saturation (S_{oi}). The imbibition K_{rw} scanning curves are plotted in Fig. 11, and they also show increasing K_{rw} with decreasing initial oil saturation. This type of data is of great importance in the understanding of the flow behavior in TZs. The impact of wettability variations within hydrocarbon TZs is not fully understood, and such data are rather scarce in the literature, especially the water relative permeability variation with S_{wi}, in which it cannot be derived from imbibition centrifuge experiments. Oil relative permeability (K_{ro}) curves were obtained in the literature by imbibition single-speed centrifuge experiments at different initial water saturations (Masalmeh 2000). The K_{ro} increased with S_{wi} at a given S_w. That is, K_{ro} increased with increasing water-wetness in the samples. Such a behavior would lead to the conclusion that the mobility of oil in the TZ can be higher than conventionally assumed. Therefore, large volumes of oil can be recovered (Masalmeh 2000). To confirm this conclusion, however, a variation in water relative permeability with S_{wi} (i.e., wettability state) is needed (as in this research study) because

Fig. 11—Water relative permeability imbibition scanning curves for the TZ samples from RRT3.

(a) Kro Scanning Curves
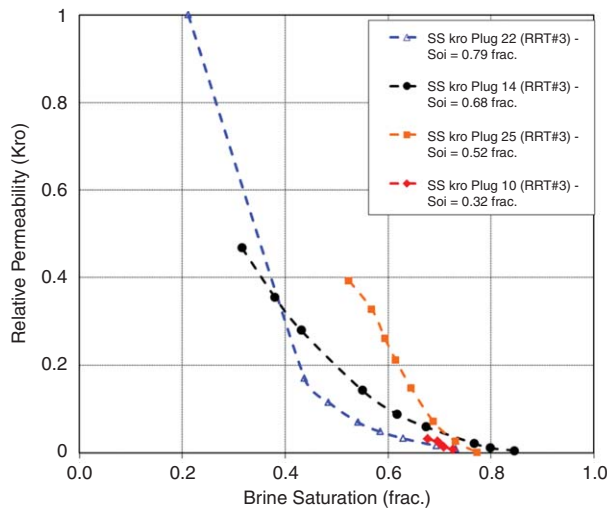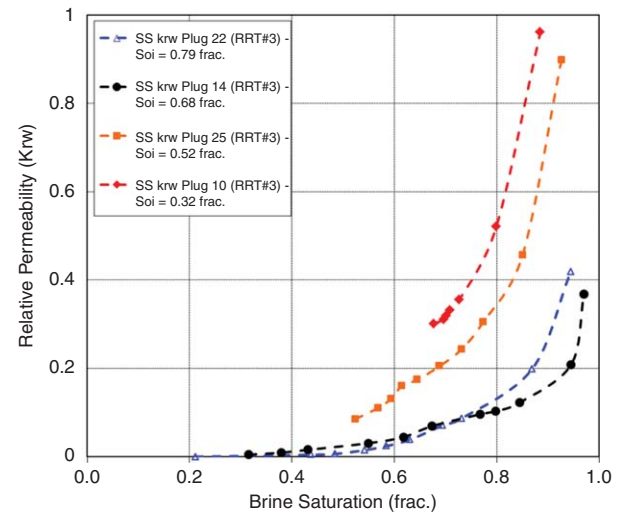
(b) Krw Scanning Curves

Fig. 12—(a) Linear-scale plot for K_{ro} scanning curves from Fig. 10b. (b) Linear-scale plot for K_{rw} scanning curves from Fig. 11.

of its significance and profound influence on waterflood efficiency (Jackson et al. 2003).

Figs. 10 and 11, respectively, present increasing K_{ro} and K_{rw} with increasing S_{wi} (i.e., decreasing S_{oi}) at a given S_w. For the larger K_{ro} curves with higher S_{wi}, this is because at low S_{wi} oil flows in both big and small pores, whereas at high S_{wi} oil flows in large pores only. This variation of K_{ro} with S_{wi} agrees with similar results obtained from imbibition single-speed centrifuge experiments (Masalmeh 2000). Fig. 10, however, shows that for Sample 25 ($S_{oi} = 0.52$), K_{ro} starts large but decreases quickly to low K_{ro} values after 0.69 S_w. This behavior occurs for low-S_{oi} samples, in which oil phase tends to lose its connectivity after a certain amount of pore space has been waterflooded. Because the oil at low S_{oi} only exists in the bigger pores, waterflood can easily sweep those pores, leaving little oil in the pore space that causes the oil to lose its connectivity and the oil permeability to drop dramatically. For even lower S_{oi} of 0.32 (Plug 10) and upon waterflood, imbibition K_{ro} drops quickly because there are fewer large pores occupied with oil. This behavior was absent with the larger S_{oi} samples because oil would be present in a wider range of pore sizes, and thus oil production occurs with a steady reduction in K_{ro} from different pore sizes; thus, we do not see a sharp decrease in K_{ro}. The oil phase can maintain good connectivity until lower oil saturations are attained. This is, of course, directly related to the oil-phase saturation distribution at the pore level. On the other hand, K_{rw} in Fig. 11 shows even more increases with decreasing S_{oi}. Hysteresis in both K_{ro} and K_{rw} may indicate nonwater-wet conditions. At low S_{wi}, there are fewer connected water-filled pores, and thus water can initially flow only in large oil-wet pores and small water-wet pores. The percentage of water-wet pores here should be critical because it will govern the fraction of water flow in the oil-wet and the water-wet pores. This will, in turn, have a direct impact on the value of K_{rw}. Therefore, at low S_{wi}, and depending on pore sizes and the wettability distribution, water can flow in large oil-wet pores. K_{rw} increases gradually and slowly as water saturation increases rapidly because of the invasion of the large pores. The increase of K_{rw} may change slope and increases rapidly when water connectivity increases until water spans the whole pore space. The start of water invasion from a higher Swi can give rise to higher K_{rw} because water would invade the larger pores only and because of the large water saturation that helps speed up water connectivity and yields larger K_{rw}. Sample 22 ($S_{oi} = 0.79$), Sample 14 ($S_{oi} = 0.68$), and Sample 25 ($S_{oi} = 0.52$) all show a change in the slope of K_{rw} increase with S_{wi}. The change of slope of the K_{rw} curve occurs at approximately 0.67 S_w for Samples 22 and 14, whereas it occurs at 0.61 S_w for Sample 25. The linear scale in **Fig. 12b** clearly shows the rapid

increase in K_{rw} at a certain S_w that must be related to the improved water connectivity as water invades the pore space.

Fig. 13a shows the scanning curve for Sample 25 ($S_{oi} = 0.52$) in between the bounding drainage and imbibition curves of Sample 22 that is believed to be of the same RRT, but permeability comparisons show that Sample 25 is at a higher permeability value than Sample 22. This could be the reason for this, or it could simply be related to pore geometry and wettability considerations. For Sample 14 ($S_{oi} = 0.68$), the scanning curve is in between the bounding drainage and imbibition curves. It is worth noting that Sample 14 is at a lower permeability value than Sample 22. From the earlier pore-geometry investigations in this paper, permeability changes may indicate variations in pore geometries, including pore sizes that may heavily affect the imbibition K_r behavior. Sample 14 gives a higher K_{rw} than Sample 22 at low S_w, although Sample 22 has a higher permeability. The higher K_{rw} of Sample 14 should be the effect of Swi, as previously explained. At a higher S_w, Sample 22 develops a higher K_{rw} than Sample 14. This is believed to be caused by the higher absolute permeability of Sample 22. From this analysis, hysteresis from K_{rw} seems to be more evidenced and influenced by pore structure and wettability than hysteresis of K_{ro}. It is clear that K_r is largely affected by S_{wi} that might be related to wettability and pore sizes. Such variation of K_r with S_{wi} could be significant in affecting production and flow behavior at the reservoir scale.

Coreflood Simulation

Numerical simulation of all coreflood experiments was performed by use of Sendra. Sendra is a proprietary simulator that is based on a two-phase 1D black-oil simulation model together with an automated-history-matching routine. The software was used to reconcile time and spatially dependent experimental data (i.e., pressure differential, fluid production, and in-situ S_w profile). This was an important exercise to provide relative permeability output data that are corrected for the effects of laboratory-scale capillary pressure. Uncorrected data may give misleading relative permeability information. Plug-sample characteristics (e.g., length, diameter, porosity, and base permeability), injected fluid properties (e.g., viscosity), coreflooding rates, brine fractions, and flooding durations were used as input parameters for the coreflood simulation. **Fig. 14** presents the PD simulated transient data for Plug 113 from RRT1: The plot to the left shows a reasonable history match for water production and pressure differential, whereas the plot to the right presents the history match of the S_w profiles. Similarly, **Fig. 15** shows the history-match data for Plug 138 from RRT 5. We show these examples to validate our drainage experimental K_r
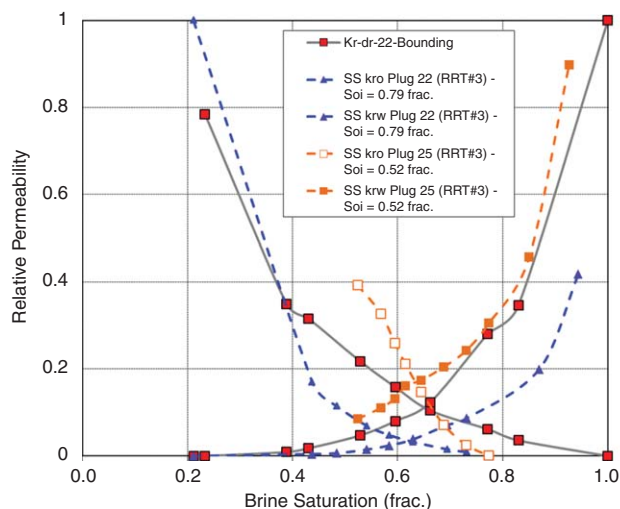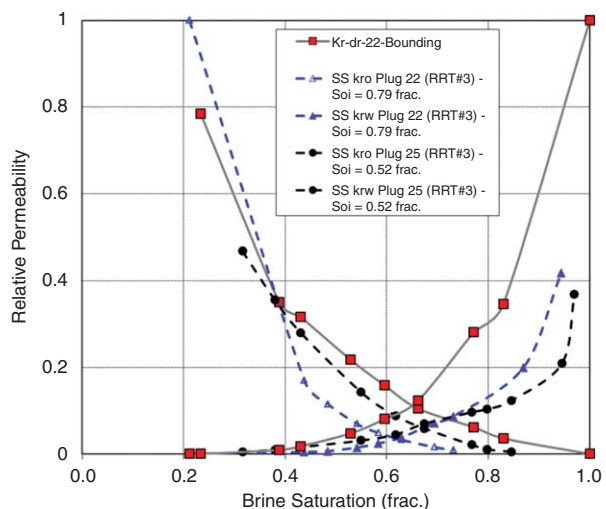
Fig. 13—(a) Scanning curve at $S_{oi} = 0.52$ plotted with drainage and imbibition bounding curves. (b) Scanning curve at $S_{oi} = 0.68$ plotted with drainage and imbibition bounding curves.
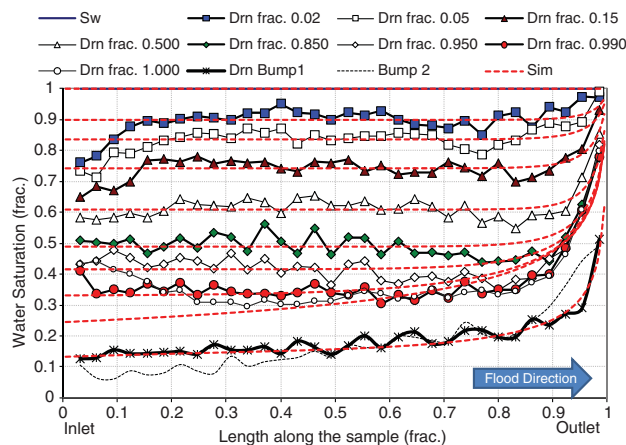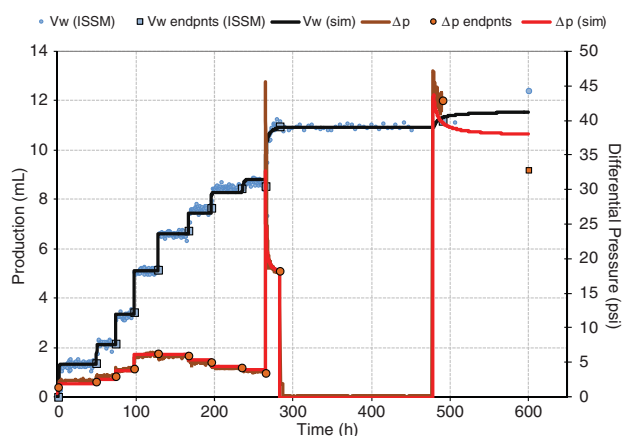

Fig. 14—PD simulated transient data for Plug 113 from RRT1. Plot to the left shows history match for water production and pressure differential. Plot to the right presents the history match of the S_w profiles.
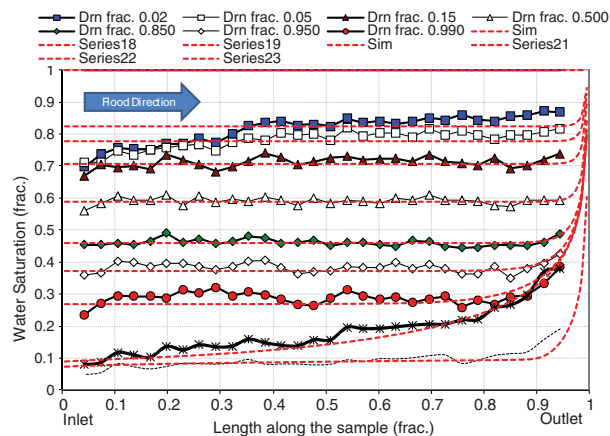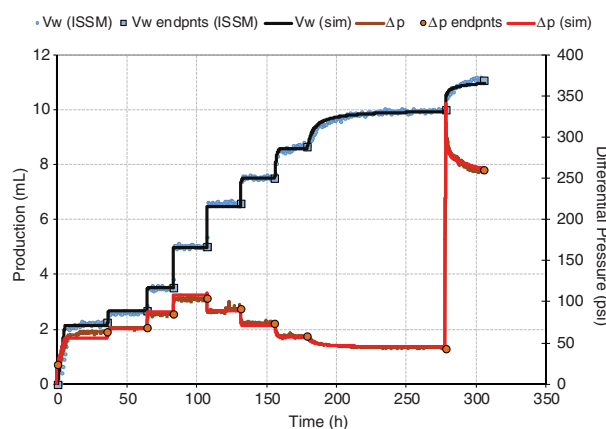

Fig. 15—PD simulated transient data for Plug 138 from RRT5. Plot to the left shows history match for water production and pressure differential. Plot to the right presents the history match of the S_w profiles.

data and thus confirm the obtained hysteresis patterns between drainage and imbibition. **Fig. 16** shows a good match between simulated relative permeability curves and the experimental data, which gives confidence in the hysteresis shapes. The figure presents both linear and semilog plots to emphasize the different hysteresis trends between RRT 1 and RRT 5 samples.

Conclusions

The following conclusions and observations can be summarized from this research study:

- DE CT scanning derives accurate porosity and mineralogy distributions along sample lengths that can enhance sample selection and improve static rock typing. Longitudinal color-scale
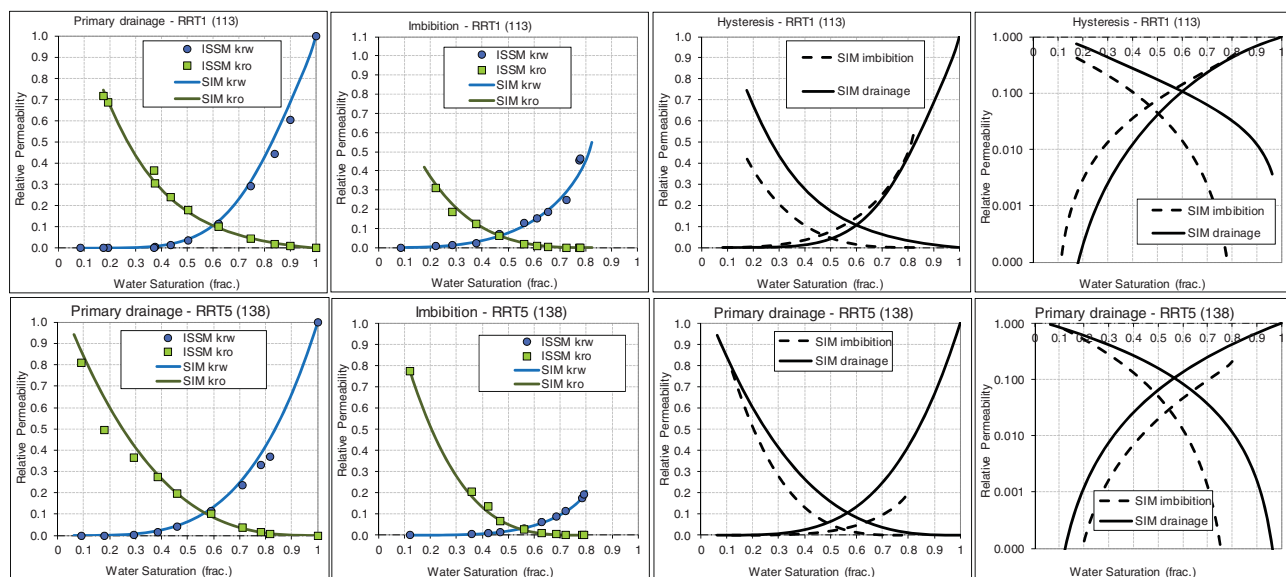
Fig. 16—Simulated relative permeability curves presented for RRT1 (113) and RRT5 (138) samples. There is a reasonable match between experimental data points and simulated curves. This validates the K_r data and thus confirms the hysteresis trends.

CT images have been essential in detecting local heterogeneity among various rock-type samples.

- The initially established static rock-typing scheme on the basis of petrophysical properties and geological description was validated by imbibition relative permeability and hysteresis trends. This validation is essential when assigning saturation functions in dynamic reservoir modeling.
- Mercury data from smaller trims can be misleading if not supported by plug measurements. This may lead to discrepancies in the static rock-typing scheme.
- Samples within the same rock type may show little variations in relative permeability curves because of local heterogeneity.
- Different rock types may not show major variations in PD K_r. This must be because of the less-complex fluid-flow mechanism governed by piston-like displacement.
- Imbibition K_r curves at representative reservoir conditions show large variations among different rock types. This effect was attributed to the combined effects of pore geometry and wettability in the complex imbibition flow.
- Imbibition K_{rw} curves show more variations with different rock types than imbibition K_{ro}. This would indicate potential differences in the flow pattern between oil and water phases in porous media.
- PD and imbibition relative permeability curves showed different hysteresis patterns on different rock-type samples that could be attributed to the combined effects of wettability and pore geometry.
- Imbibition K_r scanning curves by the SS fractional flow experiments at reservoir conditions showed trends of increasing K_{ro} with decreasing initial oil saturation. This was in agreement with previously measured K_{ro} scanning curves from centrifuge.
- Imbibition K_{rw} scanning curves were also measured and showed increasing K_{rw} with decreasing initial oil saturation. These data are not usually obtained in imbibition centrifuge programs. Such data are of great significance in affecting production and flow behavior at reservoir scale.
- Numerical simulation was performed on all the coreflood experiments presented in this paper, which showed a good match between simulated curves and experimental data. This was necessary to validate the K_r data and thus confirm the hysteresis trends.

Nomenclature

$Frac$ = fractional
F_w = water fractional flow rate
Imb = imbibition

K_r = relative permeability
K_{ro} = oil relative permeability
K_{rw} = water relative permeability
N_c = capillary number
S_{oi} = initial oil saturation
S_{or} = residual oil saturation
SS = steady state
S_w = water saturation
S_{wi} = initial water saturation
Z_{eff} = effective atomic number
μ = viscosity
σ = interfacial tension
v = velocity

Acknowledgments

References

Cuiec, L.E. 1991. *Evaluation of Reservoir Wettability and Its Effects on Oil Recovery, Interfacial Phenomena in Oil Recovery*, ed. N.R. Morrow, New York: Marcel Dekker, 319−75.

Dernaika, M.R., Kalam, M.Z., Skjæveland, S.M. et al. 2012. Hysteresis of Capillary Pressure, Resistivity Index and Relative Permeability in Different Carbonate Rock Types. *Petrophysics* **53** (5): 316−332.

Fatt, I. 1966. Microscopic Heterogeneity in Reservoir Rock and Its Influence on Reservoir Behavior. *J. Institute of Petroleum* July (7): 231.

Heaviside, J. 1991. Measurement of Relative Permeability, In *Interracial Phenomena in Oil Recovery*, ed. N.R. Morrow, New York: Marcel Dekker, 377.

Helland, J.O. and Skjæveland, S.M. 2005. Physically-Based Capillary Pressure Correlation for Mixed-Wet Reservoirs From a Bundle-of-Tubes Model. Paper SPE 89428 presented at the 2004 SPE Symposium on Improved Oil Recovery, Tulsa, Oklahoma, 17–21 April. http://dx.doi.org/10.2118/89428-MS.

Honarpour, M.M., Huang, D.D., and Al-Hussainy, R. 1995. Simultaneous Measurements of Relative Permeability, Capillary Pressure, and

Electrical Resistivity with Microwave System for Saturation Monitoring. Paper SPE 30540 presented at the SPE Annual Technical Conference and Exhibition, Dallas, Texas, 22–25 October. http://dx.doi.org/10.2118/30540-MS.

Honarpour, M., Koederitz, L. and Harvey, A.H. 1986. *Relative Permeability of Petroleum Reservoirs*, Boca Raton: CRC Press.

Jackson, M.D., Valvatne, P.H., and Blunt, M.J. 2003. Prediction of Wettability Variation and Its Impact on Waterflooding Using Pore-to-Reservoir-Scale Simulation. *J. Pet. Sci. and Eng.* **39**: 231.

Jerauld, G.R. and Salter, S.J. 1990. Effect of Pore-Structure on Hysteresis in Relative Permeability and Capillary Pressure: Pore-Level Modeling. *Transport in Porous Media* **5**: 103–151.

Masalmeh, S.K. 2000. High Oil Recoveries From Transition Zones. SPE paper 87291 presented at the SPE Abu Dhabi International Petroleum Exhibition and Conference, Abu Dhabi, UAE. 13–15 October. http://dx.doi.org/10.2118/87291-MS.

Masalmeh, S.K. 2001. Experimental Measurements of Capillary Pressure and Relative Permeability Hysteresis. Paper SCA 2001-23 presented at the SCA Conference, Edinburgh, Scotland, September.

Morgan, J.T. and Gordon, D.T. 1969. Influence of Pore Geometry on Water-Oil Relative Permeability. Paper SPE 2588 presented at the SPE 44th Annual Meeting, Denver, Colorado, September. http://dx.doi.org/10.2118/2588-MS.

Morrow, N.R. 1990. Wettability and Its Effect on Oil Recovery. *J. Pet Tech* **42** (12): 1476–1484. http://dx.doi.org/10.2118/21621-PA.

Morrow, N.R., Fischer, H., Li, Y. et al. 2008. Fundamentals of Reservoir Surface Energy As Related to Surface Properties, Wettability, Capillary Action, and Oil Recovery From Fractured Reservoirs by Spontaneous Imbibition, Final Technical Report, University of Wyoming, Laramie, Wyoming, 82071 DOE Award No.: DE-FC26-03NT15408.

Pranter, M.J., Hirstius, C.B., and Budd, D.A. 2005. Scales of Lateral Petrophysical Heterogeneity in Dolomite Lithofacies As Determined From Outcrop Analogs: Implications for 3D Reservoir Modeling. *AAPG Bull.* **89**: 645–662.

Torsaeter, O. 1988. A Comparative Study of Wettability Test Methods Based on Experimental Results From North Sea Reservoir Rocks. Paper SPE 18281 presented at the SPE Annual Technical Conference and Exhibition, Houston, Texas, 2–5 October. http://dx.doi.org/10.2118/18281-MS.

Wardlaw, N.C. 1980. The Effects of Pore Structure on Displacement Efficiency in Reservoir Rocks and in Glass Micromodels. Paper SPE 8843 presented at the First Joint SPE/DOE Symposium on Enhanced Oil Recovery, Tulsa, Oklahoma, 20–23 April. http://dx.doi.org/10.2118/8843-MS.

Wellington, S.L. and Vinegar, H.J. 1987. X-Ray Computerized Tomography. *J. Pet Tech* **39** (8): 885–898. http://dx.doi.org/10.2118/16983-PA.

Yuan, H.H. 1991. Pore-Scale Heterogeneity From Mercury Porosimetry Data. *SPE Form Eval* **6** (2): 233–240. http://dx.doi.org/10.2118/14892-PA.

Moustafa R. Dernaika has been the Manager of Ingrain Incorporated–Abu Dhabi since 2010. Before he joined Ingrain, he worked for Emirates Link ResLab LLC (Weatherford Laboratories) as the Middle East Regional Special Core Analysis (SCAL) Manager in Abu Dhabi. Dernaika holds BS and MS degrees in chemical engineering from the Middle East Technical University in Ankara, and is currently continuing his PhD study in petroleum reservoir engineering at the University of Stavanger, Norway. His current research areas include digital rock physics, dual energy CT applications, and the variation of petrophysical measurements with rock types and wettability.

Mahmoud A. Basioni has worked as a senior reservoir engineer in ADCO since 2004. He holds an MS degree in petroleum engineering from the University Texas at Austin. Basioni is interested in compositional simulation and field-development planning. He participated in several international conferences and local workshops with projects related to pressure/volume/temperature and compositional gradient, SCAL, and enhanced oil recovery.

Ahmed Dawoud, a mechanical engineer, graduated in 1974 from the Faculty of Engineering in Cairo University, Egypt. He started his E&P career with EGPC in Egypt in 1975 as a field maintenance engineer looking after a 180-MMscf/D gas desulfurization plant (10 tons/D sulfur recovery) as well as the surface-production network of flowlines and facilities in six onshore oil fields. Dawoud joined GUPCO–Egypt in 1977 as a petroleum engineer looking after surface and subsurface activities in offshore oil operations. He joined ADCO in 1981 as a petroleum engineer looking after well completion, drilling, and workover operations until 1998 when he moved to work as a reservoir engineer looking after development of new fields and the reservoir management of developed fields. As one of ADCO's experienced staff, Dawoud has been focusing on transferring the experience and knowledge he gained to younger engineers.

Mohammed Zubair Kalam is a discipline expert in special core analysis for ADCO, with 27 years of petroleum-industry experience. After completing his BSc and PhD degrees at the University of Manchester, UK, and post-doctoral research at the Oxford University, he joined BP, where he was involved in novel core-analysis research involving NMR and magnetic-resonance imaging, as well as single-phase- and multiphase-fluid flow. Kalam has been recognized with the SPE 2012 Regional Technical Award in Formation Evaluation, and is actively involved in advanced SCAL and CO_2 EOR studies and digital rock physics analyses in carbonates.

Svein M. Skjæveland is a professor of reservoir engineering at the University of Stavanger. He holds doctorate degrees in engineering physics from the Technical University of Norway and in petroleum engineering from Texas A&M University.